



# Acid strength and solvation in catalysis by MFI zeolites and effects of the identity, concentration and location of framework heteroatoms



Andrew J. Jones<sup>a</sup>, Robert T. Carr<sup>a</sup>, Stacey I. Zones<sup>a,b</sup>, Enrique Iglesia<sup>a,\*</sup>

<sup>a</sup>Department of Chemical and Biomolecular Engineering, University of California, Berkeley, CA 94720, United States

<sup>b</sup>Chevron Energy Technology Company, Richmond, CA 94801, United States

## ARTICLE INFO

### Article history:

Received 23 September 2013

Revised 25 November 2013

Accepted 9 January 2014

### Keywords:

Acid strength

Deprotonation energy

MFI

Isomorphous substitution

Methanol

Dehydration

Dimethyl ether

Solvation

Transition state selectivity

Confinement

## ABSTRACT

The effects of heteroatom identity (Al<sup>3+</sup>, Ga<sup>3+</sup>, Fe<sup>3+</sup>, or B<sup>3+</sup>), concentration and location on catalysis by MFI zeolites are examined and interpreted mechanistically using methanol dehydration rate constants and density functional theory estimates of acid strength (deprotonation energies, DPE). In doing so, we shed light on the concomitant effects of confinement and acid strength on catalytic reactivity. Rate constants (per H<sup>+</sup> from pyridine titrations during catalysis) in the first-order and zero-order kinetic regimes decreased exponentially as the DPE of MFI with different heteroatoms increased. These trends reflect a decrease in the stability of ion-pair transition states relative to the relevant precursors (H-bonded methanol and methanol dimers, respectively, for these two regimes) with decreasing acid strength and resemble those in mesoporous solid acids (e.g., polyoxometalates). Confinement effects, weaker in mesoporous solids, give larger rate constants on MFI than on POM clusters with similar DPE. Such reactivity enhancements reflect the effects of MFI voids that solvate transition states preferentially over smaller precursors via van der Waals interactions with the confining voids. Both dehydration rate constants on MFI with 0.7–2.4 H<sup>+</sup> per unit cell volume (5.2 nm<sup>3</sup>) are independent of Al or H<sup>+</sup> densities, indicating that neither H<sup>+</sup> location nor acid strength depend on acid site concentration. Higher site densities (3.6 H<sup>+</sup> per unit cell) lead to larger first-order rate constants, but do not influence their zero-order analogs. These data reflect, and in turn provide evidence for, the initial siting of H<sup>+</sup> in less constrained channel intersections and their ultimate placement within the more solvating environments of the channels themselves. Thus, the higher reactivity of Al-rich samples, often attributed to the stronger acid sites, arises instead from the ubiquitous role of zeolites as inorganic solvents for the relevant transition state, taken together with H<sup>+</sup> siting that depends on Al density. We find that heteroatom composition, but not Al density, influences acid strength in MFI, consistent with experiment and theoretical estimates of DPE, and that methanol dehydration rate constants, properly interpreted, provide relevant insights into the combined effects of acid strength and confinement on the reactivity of solid Brønsted acids.

© 2014 Elsevier Inc. All rights reserved.

## 1. Introduction

Zeolites are inorganic silica-based solids with microporous void structures and Brønsted acid sites that catalyze chemical reactions with unique reactivities and selectivities [1–4]. The isomorphous substitution of framework Si-atoms with trivalent atoms (e.g., Al<sup>3+</sup>, Ga<sup>3+</sup>, Fe<sup>3+</sup> or B<sup>3+</sup>) creates anionic charges that can be compensated by protons located on bridging O-atoms (e.g., Al–O(H)–Si). The acid strength of X-MFI samples (where X indicates the isomorphous substitution of Si<sup>4+</sup> by Al<sup>3+</sup>, Ga<sup>3+</sup>, Fe<sup>3+</sup> or B<sup>3+</sup>) depends on the identity of the trivalent framework heteroatom, as shown by deprotonation en-

ergy (DPE) estimates from density functional theory (DFT); these DPE values are much smaller for Al-MFI than for Ga-MFI, Fe-MFI or B-MFI (by 11, 23, 72 kJ mol<sup>-1</sup> [5]). Absolute and relative DPE values differ among X-MFI samples [5–9], however, depending on the type and size of the zeolite model used. These differences reflect how cluster and periodic models account for longer-range electrostatic interactions that stabilize the anionic framework after deprotonation [10,11]. Therefore, it is necessary to compare and validate calculated DPE values with experimental estimates of acid strength.

Probes of solid Brønsted acid strength include adsorption enthalpies of amines [12], alkane cracking and dehydrogenation turnover rates [13], Hammett indicators [14], <sup>13</sup>C NMR chemical shifts of adsorbed acetone [15] and Brønsted ν(OH) frequency shifts upon interactions with weak bases [16]. These probes often

\* Corresponding author. Fax: + 1 510 642 4778.

E-mail address: [iglesia@berkeley.edu](mailto:iglesia@berkeley.edu) (E. Iglesia).

lead to conflicting conclusions about the acid strength of X-MFI, at least in part, because measured properties depend on the identity of the probe molecules and on the location of protons within the microporous voids, which leads, in turn, to differences in the dispersive stabilization of adsorbed probes because of local variations in void shape and size within a given framework structure [17]. For instance, differential adsorption enthalpies of  $\text{NH}_3$  measured calorimetrically on Al-MFI and Fe-MFI zeolites are similar ( $-145 \pm 5 \text{ kJ mol}^{-1}$ ), but these samples differ markedly in their n-hexane cracking turnover rates ( $1.3 \times 10^{-3}$  vs.  $0.048 \times 10^{-3} \text{ n-C}_6\text{-H}_{14} \cdot (\text{H}^+ \cdot \text{s})^{-1}$ , 700 K) [18] leading to contradictory conclusions about their acid strength differences.

$\text{CH}_3\text{OH}$  dehydration (to dimethyl ether, DME) rate constants on  $\text{SiO}_2$ -supported Keggin polyoxometalate (POM) clusters decrease exponentially with DFT-derived DPE estimates of the clusters [19]. First-order ( $k_{\text{first}}$ )  $\text{CH}_3\text{OH}$  dehydration rate constants reflect the free energy of the DME formation transition state relative to an uncharged adsorbed  $\text{CH}_3\text{OH}$  and a gaseous  $\text{CH}_3\text{OH}$  molecule (Scheme 1). Zero-order rate constants ( $k_{\text{zero}}$ ) reflect the free energy of the same transition state, but in this instance relative to that of a cationic  $\text{CH}_3\text{OH}$  dimer (Scheme 1). The differences in charge and size between this transition state and the two reactive intermediates (H-bonded  $\text{CH}_3\text{OH}$  monomers,  $k_{\text{first}}$ ; protonated  $\text{CH}_3\text{OH}$  dimers,  $k_{\text{zero}}$ ) cause these two rate constants to depend differently on acid strength and solvation by van der Waals interactions with the surrounding void environment. Therefore, such measurements on X-MFI samples may allow the independent assessment of their acid strengths and of their heteroatom siting among the diverse local environments provided by channels and intersections within MFI frameworks. Here, we report these rate constants on X-MFI, normalized by the number of protons and their DPE values, estimated by DFT methods through extrapolation to large MFI clusters.

## 2. Methods

### 2.1. Catalyst synthesis and characterization

Al-MFI was synthesized by dissolving  $\text{Al}(\text{OH})_3$  (53%  $\text{Al}_2\text{O}_3$ , Reheis F-2000 dried gel, 0.02–0.08 g) in a solution containing demineralized

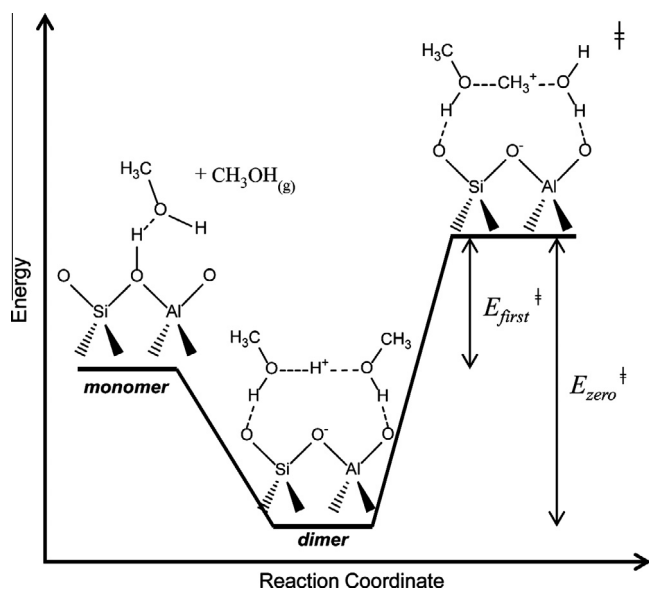
$\text{H}_2\text{O}$  (6 g), tetra-n-propyl ammonium hydroxide (TPAOH, 40 wt%, Aldrich, 1.5 g) and  $\text{NaOH}$  (1 M solution in demineralized  $\text{H}_2\text{O}$ , Fisher, 1.5 g). Amorphous  $\text{SiO}_2$  (Cab-o-sil M-5, 15 mmol) was added to the mixture, which was treated in a rotating sealed Teflon-lined vessel (43/60 Hz; Parr, 23  $\text{cm}^3$ ) held at 433 K for 6 days in a convection oven (Blue M). Solids were collected by vacuum filtration, washed with  $\text{H}_2\text{O}$  to reduce the pH to  $\sim 9$  and treated in vacuum overnight at ambient temperature. Ga-MFI and B-MFI were synthesized by the same protocols using  $\text{Ga}(\text{NO}_3)_3$  (nonahydrate, 99.9%, Aldrich, 0.03 g) and  $\text{Na}_2\text{B}_4\text{O}_7$  (decahydrate, >99.5%, Aldrich, 0.06 g) instead of  $\text{Al}(\text{OH})_3$ . The same procedure was used to prepare Fe-MFI, using  $\text{Fe}(\text{NO}_3)_3$  (nonahydrate, >99.9%, Baker, 0.12 g), TPAOH (40 wt%, Aldrich, 2.4 g),  $\text{NaOH}$  (1 M solution in demineralized  $\text{H}_2\text{O}$ , Fisher, 0.5 mmoles), demineralized  $\text{H}_2\text{O}$  (4 g) and Cab-o-sil M-5 (20 mmol). Other Al-MFI samples were obtained from a commercial source (Table 1).

Samples were analyzed by scanning electron microscopy (JEOL JSM-6700F) and X-ray diffraction (Siemens D-500;  $\text{Cu K}_\alpha$  radiation) to determine their size and framework identity. Si, Al, Ga, Fe, B and Na contents were measured by inductively coupled plasma optical emission spectroscopy (ICP-OES; Galbraith Laboratories; Supporting information). The fraction of Al-atoms in tetrahedral and octahedral coordination was determined from  $^{27}\text{Al}$  magic angle spinning NMR lines at 55 ppm and 0 ppm, respectively (details in Section S.2 of the Supporting information).

### 2.2. Catalytic rate measurements

MFI samples were pressed, crushed using a mortar and pestle, and sieved (to retain 180–250  $\mu\text{m}$  aggregates), and then diluted with  $\text{SiO}_2$  (Cab-o-sil HS-5, washed with 1.0 M  $\text{HNO}_3$ , 180–250  $\mu\text{m}$  pellets) to maintain a sample mass larger than >0.025 g. Samples were held on a coarse quartz frit within a tubular packed-bed quartz reactor (7.0 mm i.d.) and their mass (5–220 mg) was adjusted to conversions below 5%. The bed temperature was kept constant using a resistively heated three-zone furnace (Applied Test Systems Series 3210) and Watlow controllers (EZ-ZONE PM Series); it was measured using a K-type thermocouple in contact with the outer surface of the quartz tube at the center of the catalyst bed.

All samples were treated in flowing 5%  $\text{O}_2/\text{He}$  mixture ( $83.3 \text{ cm}^3 \text{ g}^{-1} \text{ s}^{-1}$ , 99.999%, Praxair) by heating to 773 K (at  $0.025 \text{ K s}^{-1}$ ), holding at 773 K for 2 h and cooling to 433 K before catalytic measurements. Liquid  $\text{CH}_3\text{OH}$  (99.8%, Sigma-Aldrich) was introduced via heated lines (>373 K) into He flow (99.999%, Praxair) using a syringe pump (Cole-Palmer 780200C series). Reactant, product and titrant concentrations were measured by gas chromatography (Agilent 6890N GC) using a DB-Wax capillary column (0.320 mm ID  $\times$  30 m  $\times$  0.50  $\mu\text{m}$  film; J&W Scientific) and



**Scheme 1.** Illustration of the relationships between the energies of H-bonded  $\text{CH}_3\text{OH}$  monomers, protonated dimers and cationic DME formation transition states reflected in measured first-order ( $E_{\text{first}}^{\ddagger}$ ) and zero-order ( $E_{\text{zero}}^{\ddagger}$ )  $\text{CH}_3\text{OH}$  dehydration rate constants.

**Table 1**  
Zeolite sample information.

Zeolite	Provenance	Si/T <sup>a</sup>	H <sup>+</sup> /T <sup>b</sup>	H <sup>+</sup> /T <sup>c</sup>	%T <sub>Td</sub> <sup>d</sup>
H-[Al]-MFI-1	Commercial	16.6	0.65	0.52	88
H-[Al]-MFI-2	This work	22.8	0.27	0.33	85
H-[Al]-MFI-3	Commercial	29.2	0.77	0.72	89
H-[Al]-MFI-4	Commercial	43.8	1.03	0.89	89
H-[Al]-MFI-5	This work	51.9	0.59	–	87
H-[Al]-MFI-6	This work	117.6	0.86	–	96
H-[Ga]-MFI	This work	108.7	1.09	–	–
H-[Fe]-MFI	This work	61.1	0.85	0.68	–
H-[B]-MFI	This work	75.3	0.25	–	–

<sup>a</sup> Determined from elemental analysis (ICP-OES; Galbraith Laboratories).

<sup>b</sup> Determined from pyridine titrations during  $\text{CH}_3\text{OH}$  dehydration reactions at 433 K.

<sup>c</sup> Determined from  $\text{NH}_4^+$  decomposition.

<sup>d</sup> Fraction of Al in tetrahedral coordination (%T<sub>Td</sub>) determined from  $^{27}\text{Al}$  MAS NMR.

flame ionization, and mass spectrometric detection (MKS Spectra Minilab). Dimethyl ether and water were the only products observed at all reaction conditions.

CH<sub>3</sub>OH dehydration rates (per mass) on SiO<sub>2</sub> (0.2114 g) and silicalite-1 (SIL-1, 0.2236 g, synthesized using previously developed protocols [20] and Ludox AS-40) were <0.03 of those on Al-MFI at all conditions; on SIL-1, such rates were ~20% of those measured on H-[B]-MFI (at 55 kPa CH<sub>3</sub>OH). These SIL-1 rates were subtracted from measured H-[B]-MFI rates to account for contributions from the purely siliceous framework. Rates were measured periodically at a given reaction condition (10 kPa CH<sub>3</sub>OH, B-MFI; 0.6 kPa CH<sub>3</sub>OH, other X-MFI; 433 K); no deactivation was detected on Fe-, B- and some Al-MFI samples (Si/Al = 22.8, 51.9 and 117.6). Al-MFI (Si/Al = 29.2 and 43.8) and Ga-MFI samples were corrected for slight deactivation (<15% over >5 h). Athena Visual Studio [21] was used to regress rate data to the functional form of the mechanism-based rate equations and to determine 95% confidence intervals.

### 2.3. Chemical titration of sites with pyridine and decomposition of exchanged NH<sub>4</sub><sup>+</sup> cations

Brønsted acid sites were measured using pyridine (99.9%, Sigma-Aldrich) as a titrant during CH<sub>3</sub>OH dehydration at 433 K. Pyridine (0.3–3.0 Pa) was introduced after establishing steady-state CH<sub>3</sub>OH dehydration rates (10 kPa CH<sub>3</sub>OH, B-MFI; 1.1 kPa CH<sub>3</sub>OH on other X-MFI) by introducing a pyridine-CH<sub>3</sub>OH liquid mixture into the reactor. Titrant effluent concentrations were measured using the chromatographic protocols described above. The number of protons in each sample was determined from the cumulative titrant uptakes of pyridine required to fully suppress CH<sub>3</sub>OH dehydration rates (assuming a 1:1 pyridine:H<sup>+</sup> adsorption stoichiometry).

Protons were also measured by decomposition of NH<sub>4</sub><sup>+</sup> (to form NH<sub>3</sub>) on NH<sub>4</sub><sup>+</sup>-exchanged samples, prepared by treating the H<sup>+</sup> form of MFI in flowing dry air (2.5 cm<sup>3</sup> g<sup>-1</sup> s<sup>-1</sup>, UHP Praxair; heating to 823 K at 0.025 K s<sup>-1</sup>, 4 h hold) and adding these samples to 0.1 M NH<sub>4</sub>NO<sub>3</sub> (>98%, Sigma-Aldrich; 1 g zeolite per 300 cm<sup>3</sup>) while stirring at 353 K for 4 h. The solids were recovered by filtration and the exchange procedure was carried out two more times. After the third exchange, samples were filtered, washed with 300 cm<sup>3</sup> demineralized H<sub>2</sub>O and allowed to stand in ambient air. NH<sub>4</sub><sup>+</sup>-exchanged samples (0.05–0.13 g) were placed within the reactor described in Section 2.2 and heated to 923 K (at 0.833 K s<sup>-1</sup>) in flowing He (2.5 cm<sup>3</sup> g<sup>-1</sup> s<sup>-1</sup>, 99.999%, Praxair) and Ar (0.83 cm<sup>3</sup> g<sup>-1</sup> s<sup>-1</sup>, 99.999%, Praxair) and held for 1 h. A heated, Si-coated stainless steel capillary (420 K, 0.254 mm i.d., 183 cm length) was placed directly after the samples and connected to a mass spectrometer (MKS Spectra Minilab) to measure NH<sub>3</sub> concentrations in the effluent stream. The intensities for NH<sub>3</sub> (17, 16 amu), H<sub>2</sub>O (18, 17 amu) and Ar (40 amu) ions were acquired every 4 s.

### 2.4. Density functional theory calculations of deprotonation energy

Geometry optimizations were performed on neutral (ZH) and deprotonated (Z<sup>-</sup>) clusters with the hybrid functional ωB97X-D [22] using the double-ζ, polarized valence 6-31G(d,p) basis set implemented in the Gaussian software package [23]. Wave functions were converged to 1.0 × 10<sup>-6</sup> hartree and structures were optimized until the root-mean-square force was less than 3 × 10<sup>-4</sup> hartree bohr<sup>-1</sup>. Single-point calculations on the resulting geometries were performed at the ωB97X-D/6-311++G(3df, 3pd) level to test the effects of a larger basis set.

DPE values were calculated using cluster models derived from the MFI crystal structure [24] and terminated with H-atoms (Si-H bond lengths fixed at 0.1455 nm [25]) to replace terminal O-atoms while maintaining charge neutrality. Terminal SiH<sub>x</sub> atoms

were fixed during geometry optimizations while all other atoms were allowed to relax, thus preventing the energetic relaxation of clusters into structures unrelated to the periodic crystalline framework [27]. Si-H bonds were used instead of Si-O-H to terminate clusters, because Si-O-H leads to unrealistic electrostatic destabilization and large DPE values [11]. The T12 site of MFI, according to the numbering convention of Olson et al. [24], was considered as the heteroatom substitution site for all clusters, with a H<sup>+</sup> located in the X12-O20(H)-Si3 position (where X = Al, Ga, Fe or B) [25,27]. The resulting H<sup>+</sup> resides in the void created by the intersection of the straight and sinusoidal channels in MFI.

MFI clusters with one X heteroatom and 5, 8, 11, 20, 27, 38 or 51 tetrahedral atoms (denoted as 5T, etc.) were extracted from periodic MFI structures built from coordinates derived from X-ray diffractograms [24] to look at the effect of increasing the number of Si and O-atoms that lie between the acid site and the terminal Si-atoms on DPE. The clusters with 5 and 38 T-atoms after relaxation are depicted in Fig. 3 (heteroatom sites identified; other clusters in Section S.3 of the Supporting information). Clusters with Fe heteroatoms were calculated with a spin multiplicity of six since Fe<sup>3+</sup> has a high spin ground state (d<sup>5</sup>) in tetrahedral coordination [8] and because spin polarized energy calculations on 5T clusters indicated that this was the most stable electronic configuration.

DPE values represent the energy required to heterolytically cleave H-atoms from the zeolite framework (HZ) to form a noninteracting H<sup>+</sup> and a zeolite framework anion, Z<sup>-</sup>. DPE values were calculated as the energy difference between these deprotonation products and the neutral starting structure:

$$E_{DPE} = E_{Z^-} + E_{H^+} - E_{HZ} \quad (1)$$

where  $E_{Z^-}$ ,  $E_{H^+}$  and  $E_{HZ}$  are the electronic energies of the deprotonated zeolite anion, a bare proton and the neutral Brønsted acid, respectively.

### 2.5. Infrared detection of Brønsted acid sites

Infrared spectra were collected in transmission mode using self-supporting wafers (~5–15 mg cm<sup>-2</sup>) and a quartz vacuum cell with NaCl windows. Spectra were measured in the 4000–400 cm<sup>-1</sup> range with a 2 cm<sup>-1</sup> resolution using a Nicolet NEXUS 670 spectrometer equipped with a Hg-Cd-Te (MCT) detector by averaging 64 scans. Samples were treated by heating to 723 K (0.033 K s<sup>-1</sup>) in dry air (1.67 cm<sup>3</sup> s<sup>-1</sup>, zero grade, Praxair), holding for 2 h and then cooling to 433 K. Samples were evacuated using a diffusion pump (<0.01 Pa dynamic vacuum; Edwards E02) before collecting spectra. All spectra were normalized by the intensity of the Si-O-Si overtones (2100–1750 cm<sup>-1</sup>).

## 3. Results and discussion

### 3.1. CH<sub>3</sub>OH dehydration on X-MFI: Proton site counts and kinetic effects of CH<sub>3</sub>OH pressure

Fig. 1 shows CH<sub>3</sub>OH dehydration rates (433 K; per heteroatom from elemental analysis; Table 1) as a function of pyridine titrant uptakes on X-MFI samples. CH<sub>3</sub>OH dehydration rates decreased linearly with the amount of pyridine adsorbed (Fig. 1); rates did not increase when pyridine was removed from the inlet stream, indicating that pyridine irreversibly titrates all sites active for CH<sub>3</sub>OH dehydration. Pyridine (0.6 nm kinetic diameter [28]) can diffuse through MFI channels (10-MR channels, ~0.55 nm diameter) and is protonated by Brønsted acid sites, rendering such sites unreactive for CH<sub>3</sub>OH dehydration, but it can also coordinate to Lewis acid sites in zeolites [29]. Larger 2,6-di-*tert*-butylpyridine (1.05 nm diameter) molecules selectively titrate Brønsted acid

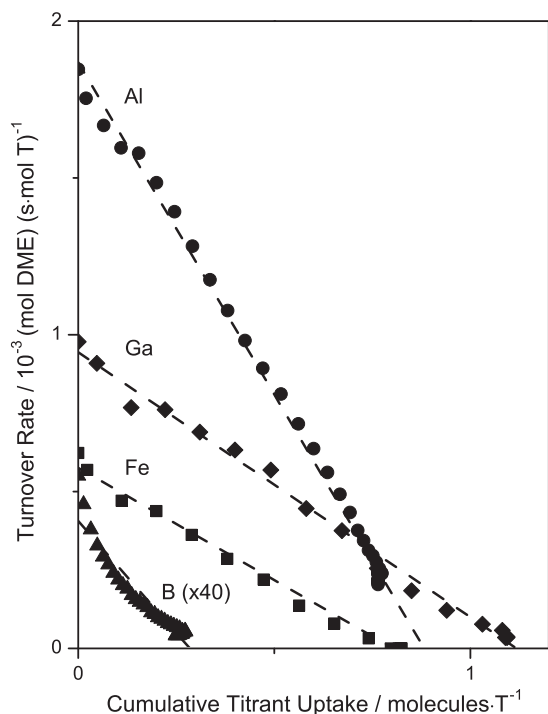


**Fig. 1.** CH<sub>3</sub>OH dehydration rates at 433 K (per metal atom (*T*) measured from elemental analysis, Table 1) as a function of cumulative pyridine on H-[Al]-MFI-6 (●), H-[Ga]-MFI (◆), H-[Fe]-MFI (■) and H-[B]-MFI (▲) (1.1 kPa CH<sub>3</sub>OH and 0.6 Pa pyridine for Al, Ga, and Fe substituted MFI samples; 10 kPa CH<sub>3</sub>OH and 1.2 Pa pyridine for B-MFI). Dashed lines are linear regression fits of the data.

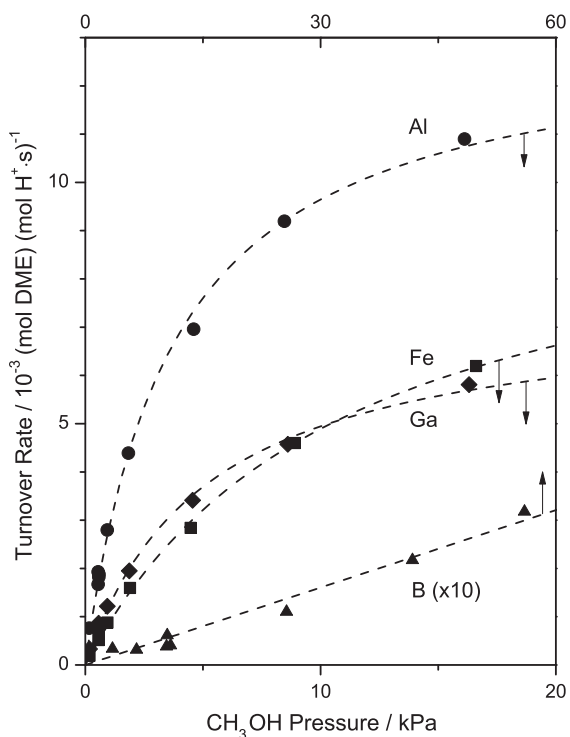


**Fig. 2.** CH<sub>3</sub>OH dehydration turnover rates at 433 K normalized by pyridine uptakes on H-[Al]-MFI-6 (●), H-[Ga]-MFI (◆), H-[Fe]-MFI (■) and H-[B]-MFI (▲). Dashed curves represent regression of data points to Eq. (2).

sites [30], but did not decrease rates on H-[Al]-MFI-1, indicating that such titrants cannot access H<sup>+</sup> within MFI channels and that

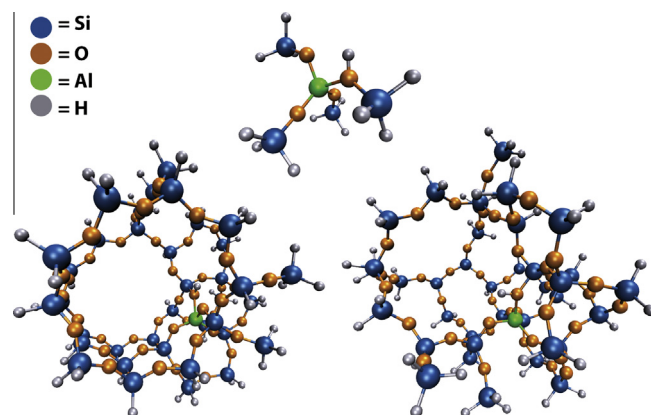


**Fig. 3.** Optimized geometries of H<sub>13</sub>Si<sub>4</sub>Al<sub>1</sub>O<sub>3</sub> (5T; top) and H<sub>55</sub>Si<sub>37</sub>Al<sub>1</sub>O<sub>49</sub> (38T; bottom) H-Al-MFI clusters (geometries for 8, 11, 20, 27 and 51 T-atom clusters provided in the Supporting information). The 38 T-atom cluster is shown in two orientations, looking down the 10-MR straight channel (left) and looking down the 10-MR sinusoidal channel at the void created from channel intersections (right). Atom colorings are as follows: H in gray, Si in blue, O in orange and Al in green. (For interpretation of the references to color in this figure legend, the reader is referred to the Web version of this article.)

the fraction of H<sup>+</sup> at external MFI surfaces is inconsequential for catalysis. We compare pyridine uptakes (Table 1) with ex situ H<sup>+</sup> counts from the thermal decomposition of the NH<sub>4</sub><sup>+</sup>-form of these zeolites to determine the quantity of Lewis acid sites from the difference of their values; these site counts are selective to Brønsted acid sites because NH<sub>4</sub><sup>+</sup> cations in solution replace H<sup>+</sup> during exchange but do not coordinate to Lewis acid sites. NH<sub>4</sub><sup>+</sup> and pyridine uptakes were similar (within a factor of 0.8; Table 1) indicating that pyridine adsorbs negligibly at any Lewis acid sites that may be present on these samples. The negligible adsorption of pyridine on Lewis acid sites and the near-complete suppression of DME formation rates by pyridine titrants on these samples indicate that Lewis acid sites do not contribute detectably to CH<sub>3</sub>OH dehydration rates on these samples.

DME formation rates were fully suppressed by contact with pyridine on Ga-MFI and Fe-MFI samples, but small residual rates (~10% of initial rates) were detected after saturation titrant uptakes on B-MFI and on H-[Al]-MFI-6 (Fig. 1). The small residual rates after titration do not appear to be the result of Lewis acid sites because pyridine titrants will also coordinate with Lewis acid sites if they are present [29]. They may instead reflect DME formation on H<sup>+</sup> that are accessible to CH<sub>3</sub>OH reactants but inaccessible to pyridine titrants as the result of adsorbed pyridine molecules that hinder the diffusion of pyridine molecules to reactive H<sup>+</sup>, or due to structural defects that occlude pyridine molecules from certain voids. Therefore, the total number of protons on each sample was estimated by extrapolating titrant uptakes to zero CH<sub>3</sub>OH dehydration rates. They are reported in Table 1 along with sample provenance, chemical composition and Al coordination determined from <sup>27</sup>Al MAS NMR.

Proton counts (per heteroatom) from pyridine titrations and NH<sub>4</sub><sup>+</sup> decomposition were smaller than unity (except for H-[Al]-MFI-4 and H-[Ga]-MFI; Table 1), indicating that some heteroatoms do not have associated protons of sufficient strength to protonate pyridine irreversibly. This may reflect distorted heteroatoms with tetrahedral or octahedral coordination or extra-framework phases [31,32] that lack reactive protons. <sup>27</sup>Al MAS NMR data show that some samples contain more framework Al-atoms than protons (e.g., 0.88 Al<sub>Td</sub>/Al<sub>Tot</sub> vs. 0.65 H<sup>+</sup>/Al<sub>Tot</sub>, H-[Al]-MFI-1, Table 1), but NMR studies use samples hydrated at ambient conditions, which can re-form tetrahedral Al centers [33]. This may lead to Al species that are tetrahedral during NMR experiments but do not contain

Brønsted acid sites after relevant catalyst pretreatment and reaction conditions [34]. The ubiquitous and variable  $H^+/Al_{Td}$  substoichiometry makes tetrahedral Al sites an equivocal surrogate for the number of protons, which must be determined instead by using specific titrants, whenever possible as catalysis takes place [34]. Here, we use pyridine uptakes, which titrate Brønsted acid sites in these samples, as an estimate of the number of protons in calculating turnover rates.

$CH_3OH$  dehydration turnover rates (per  $H^+$ ) are shown in Fig. 2 as a function of  $CH_3OH$  pressure on X-MFI samples. Turnover rates on Al-MFI, Ga-MFI and Fe-MFI samples increased linearly with  $CH_3OH$  pressure below 3 kPa  $CH_3OH$  and then more gradually consistent with a Langmuir-type rate equation:

$$\frac{r}{[H^+]} = \frac{k_{first}[CH_3OH]}{1 + \frac{k_{first}}{k_{zero}}[CH_3OH]} \quad (2)$$

Here,  $k_{first}$  and  $k_{zero}$  are the regressed first-order and zero-order parameters that give rise to the dashed curves in Fig. 2. Dehydration turnover rates on B-MFI samples increased linearly with  $CH_3OH$  pressure at all pressures (up to 60 kPa  $CH_3OH$ ) so that only  $k_{first}$  could be measured.

Turnover rates were influenced by the identity of the heteroatom (Al, Ga, Fe, B) at low pressures (<10 kPa  $CH_3OH$ ) in a manner consistent with their different DPE values (Section 3.2) and with the expectation that stronger acids, with a more stable conjugate anion, would lead to lower activation energies for reactions mediated by ion-pair transition states [35]. Turnover rates ultimately become zero-order in  $CH_3OH$  at higher pressures on Al-MFI, Ga-MFI and Fe-MFI; these constant values confirm the absence of mass transfer effects, a conclusion supported by the similar turnover rates measured on Al-MFI samples with different Si/Al ratios and crystal sizes (Section 3.4).

Next, we assess the acid strength of X-MFI samples using theoretical DPE values and use these values in Section 3.3 to interpret and compare rate constants in terms of the relative contributions of dispersive and electrostatic forces on the stability of the transition state and its relevant precursors.

### 3.2. Density function theory calculations of deprotonation energy

DFT-derived DPE values have been reported with contradictory results for zeolites using periodic [36,37], embedded cluster [38,39] and free cluster [5–8] models. Periodic boundary conditions give rise to spurious electrostatic interactions among the charge defects formed by deprotonation in neighboring cells [40–42], which have remained uncorrected in these previous studies. Embedding approaches connect cluster models, treated locally using rigorous quantum mechanics (QM), to a potential field that represents the periodic zeolite via linking H-atoms [39]. It remains unclear, however, how the presence and position of these linking atoms affect calculated DPE values as they have been shown to do for small clusters [11,35]. In addition, the wave function of the cluster region is not influenced directly by the charge distribution of the potential region [38], which may be important for describing the long-range electrostatics important in anion energy calculations of clusters [10,11].

Cluster models represent small portions of larger periodic structures, which do not accurately represent the O:Si stoichiometry in zeolites; these clusters must be terminated abruptly in a way that influences DPE values [11,35]. Large clusters mitigate the artifacts created by terminal atoms on the stability of the cluster to deprotonation [11], and therefore, the use of large clusters represents the most reliable strategy to explore these electrostatic effects, albeit at significant computational expense. DPE values (calculated at the HF/3-21G level) oscillate with the monotonic addition of Si

and O shells around an Al-atom in MFI for cluster models up to 8 tetrahedral atoms (T-atoms) in size [11], but DPE values slowly converge to constant values with increasing cluster size [10]. The large clusters required to approach realistic electrostatic interactions (>46 T-atoms) [10] have not been used, to our knowledge, to calculate DPE values for MFI with heteroatoms other than Al, an approach that we follow here in order to assess the effects of acid strength on  $CH_3OH$  dehydration rate constants on X-MFI.

DPE values are shown in Fig. 4 as a function of the reciprocal of the number of T-atoms in the clusters for each X-MFI composition. DPE values decreased with increasing cluster size (5–51 T-atoms), suggesting that either (i) charge is transferred (delocalized) many atom distances away from the anion, or (ii) O-, Si- and terminal H-atoms become polarized in the clusters through long-range electrostatic interactions with the anion; we will henceforth refer to these two scenarios as delocalization and polarization, respectively. These size effects are strongest for B-MFI, which shows the highest DPE value and the least stable anionic cluster (DPE decreased by 132 kJ mol<sup>-1</sup> from 5T to 38T B-MFI clusters). This may reflect the small size of B<sup>3+</sup> cations (effective ionic radius of 0.027 nm [43], absolute hardness of 111 eV [44]), which stabilizes negative charge less effectively than larger cations (e.g., Al<sup>3+</sup> with an effective ionic radius of 0.054 nm [43], absolute hardness of 46 eV [44]), causing DPE values to be more sensitive to long-range effects that are more accurately described as the size of the clusters increase. The effects of the size of the clusters used in DPE estimates weaken for larger clusters (>20 T-atoms; Fig. 4), suggesting that electrostatic interactions rigorously approach those found in actual zeolite lattices, as discussed by Brand et al. [10], and that the effects of delocalization or polarization do not extend far beyond the second coordination sphere of O-atoms from the heteroatom (where the first coordination sphere of O-atoms is defined as that containing O-atoms bonded directly to the heteroatom).

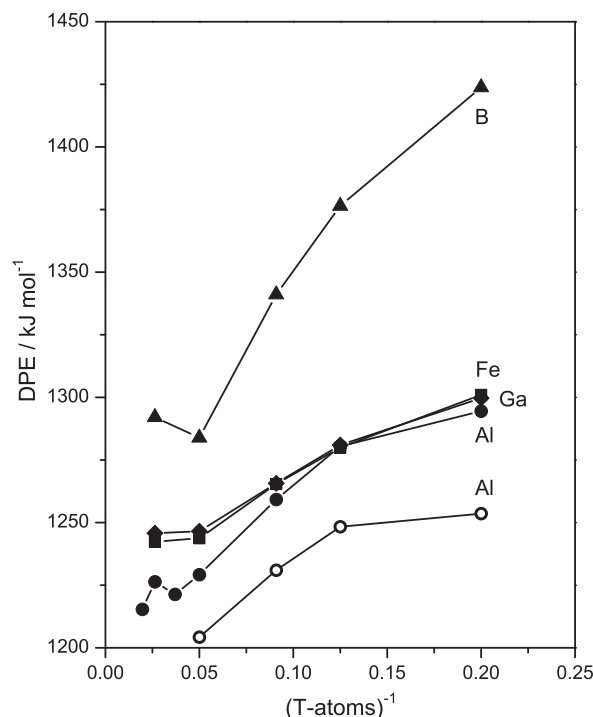


Fig. 4. Calculated DPE values for Al (●), Ga (◆), Fe (■) and B (▲) heteroatoms in MFI at the T12 site as a function of cluster size calculated with the  $\omega$ B97X-D exchange correlation functional and a 6-31G(d, p) basis set. Open circles are single-point calculations of optimized Al-MFI clusters with the 6-311++G(3df, 3pd) basis set.

Next, we consider the influence of basis set size on DPE trends with cluster size in Al-MFI clusters (Fig. 4). Increasing the basis set size allows enhanced electron density polarization and diffuseness, and may impact the ability of clusters to delocalize or polarize charge. Increasing the 6-31G(d, p) basis set to the near-complete 6-311++G(3df, 3pd) decreased DPE values by 41 and 25 kJ mol<sup>-1</sup> for Al-MFI with 5T and 20T clusters, respectively (Fig. 4). The effects of the larger basis set decrease with increasing cluster size; extrapolation of the difference in DPE values calculated with the two basis sets to larger clusters suggests that DPE values are 19 kJ mol<sup>-1</sup> larger for 6-31G(d, p) than for 6-311++G(3df, 3pd) basis sets for clusters larger than 38 T-atoms (Supporting information). This suggests that DPE values of 51T Al-MFI clusters calculated at the 6-311++G(3df, 3pd) level are ~1200 kJ mol<sup>-1</sup>, a value also reported for Al-MFI using embedding cluster methods (1200 kJ mol<sup>-1</sup>) [38]. This value also resembles that inferred from 2-butanol dehydration rate constants measured on POM clusters and another aluminosilicate (H-Al-BEA; 1185 kJ mol<sup>-1</sup>) [45]. The systematic effects of cluster size on DPE suggest that both basis sets give similar DPE differences among X-MFI samples; DPE comparisons among solid acids of different types (e.g., zeolites and heteropolyacids), however, require near-complete basis sets, similar structural models (e.g., cluster vs. periodic) and the same level of theory (e.g., DFT vs. MP2).

The strong and systematic effects of cluster size on DPE (>130 kJ mol<sup>-1</sup> for B-MFI clusters from 5T to 38T) seem surprising for insulating frameworks where considerable charge transfer is not expected. The origins of these cluster size effects were probed by examining the electron density differences between neutral and deprotonated structures. Fig. 5a shows the electron density distribution of the neutral (HZ) and anionic (Z<sup>-</sup>) 38T Al-MFI clusters (with Al at the origin). The locations of peaks in Fig. 5a align with the locations of the first (Al–O<sup>+</sup>) and second (Al–O–Si<sup>+</sup>) coordination spheres of O-atoms away from the heteroatom (the

asymmetry of the cluster prevents the perfect assignment of subsequent electron density peaks because the O-atoms are located at various positions), consistent with the negative charge located predominantly at these locations. Deprotonation of the cluster (Fig. 5a) did not lead to detectable changes in the position of these peaks, but caused a large increase in electron density at 0.8 nm, which corresponds to the position of the second coordination sphere of O-atoms. This suggests that atom displacements resulting from deprotonation do not significantly influence the electron density because these would result in changes in the positions of peaks in Fig. 5a. Instead, the increase in electron density upon deprotonation at the second coordination sphere O-atoms reflects either (i) charge delocalization or (ii) charge polarization of the atom or Si–O bond, which we discuss next.

The difference between electron densities for protonated and deprotonated 38T Al-MFI clusters (Fig. 5a) is shown in Fig. 5b. A positive feature indicates a loss of electron density at that position. The weak feature at ~0.3 nm shows that the O-atoms bonded to the Al heteroatom acquire only a small negative charge upon deprotonation and that this negative charge resides predominantly at more distant O-atoms (0.8 nm) in the second O-coordination sphere. The loss of electron density at 0.6 nm corresponds to the first coordination sphere of Si-atoms (Al–O–Si<sup>+</sup>). The similar size of the negative features at 0.6 and 0.8 nm, respectively, suggests that electron density moves from Si-atoms in the first coordination sphere (Al–O–Si<sup>+</sup>) to O-atoms in the second coordination sphere (Al–O–Si–O<sup>-</sup>) upon deprotonation. Therefore, the most evident changes in electron density upon deprotonation arise from the polarization of charge along the Si–O bond, which places a larger electron density on the second coordination sphere O-atoms and removes some electron density from the first coordination sphere Si-atoms. The delocalization of electron density near atoms close to the heteroatom, however, seems negligible, in view of the lack of strong features below 0.6 nm (Fig. 5b), which would indicate a change in electron density near the Al heteroatom. The polarization

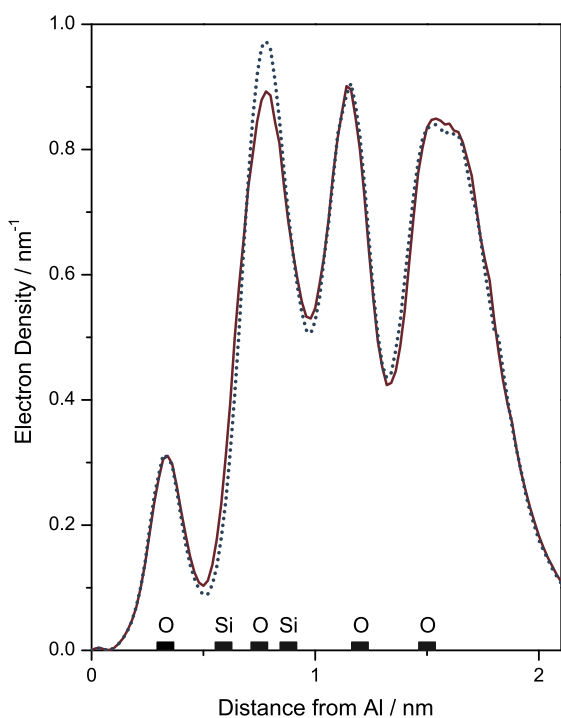


**Fig. 5a.** Electron density distribution of a 38 T-atom Al-MFI cluster as a function of the distance from Al before (solid line) and after (dotted line) deprotonation. Al is located at the origin; average positions of some O-atoms and Si-atoms are identified for clarification.

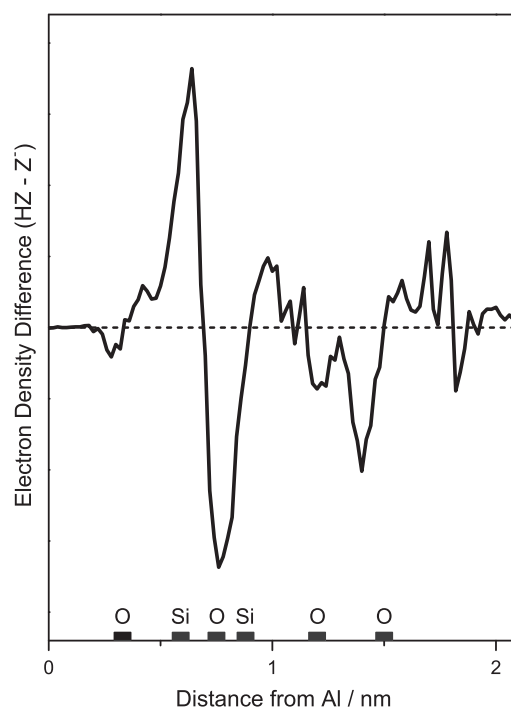


**Fig. 5b.** Difference in the electron densities between the protonated (HZ) and deprotonated (Z<sup>-</sup>) 38 T-atom Al-MFI clusters (Fig. 5a). Al is located at the origin; average positions of some O-atoms and Si-atoms are identified for clarification. Positive features indicate a loss of electron density in that region.

of the Si–O bond may be the result of the loss of the electrostatic potential of the  $H^+$  cation, which removes the long-range electrostatic attraction of electrons to the  $H^+$  location, therefore allowing electrons to concentrate on distant but more electronegative O-atoms (instead of Si-atoms).

Changes in the cluster electron density upon deprotonation at distances beyond 1 nm from the Al center are evident in Fig. 5b. These features are smaller than those residing at the second coordination sphere O-atoms. A Bader charge analysis [46] (Section S.5 of the Supporting information) shows that individual Si and O charges change by less than a factor of 1.05 upon deprotonation, consistent with the low dielectric constants for aluminosilicates [47] and their consequent resistance to charge delocalization. We conclude that the deprotonation of clusters induces changes in the polarization of Si–O bonds and atoms (instead of a long-range delocalization of charge) and thereby changes the ability of the cluster to stabilize charge. DFT-derived DPE values converge only for cluster models larger than 20 T-atoms, in which second coordination sphere O-atoms are not connected to terminal Si–H bonds, suggesting that polarization up to the second O-atom coordination sphere is essential for stabilization of the negative charge formed upon deprotonation and therefore for accurate DPE calculations in zeolites. We note that only minor changes to the electron density are observed at the Al–O bonds, which may explain the consistency of DPE values calculated here and with embedded approaches, which allow for the polarization of the potential region by the anionic structure, but do not allow for the influence of the potential region on the wave function of the QM cluster.

### 3.3. Mechanistic origins of $CH_3OH$ dehydration rate constants

Next, we interpret measured  $CH_3OH$  dehydration rate constants ( $k_{first}$  and  $k_{zero}$ ) in terms of elementary steps and their rate and equilibrium constants. DFT calculations and measured  $CH_3OH$  dehydration turnover rates indicate that  $CH_3OH$  dehydration proceeds via direct routes involving H-bonded monomers and protonated dimers on W-based polyoxometalate clusters (POM) [19]. Protonated  $CH_3OH$  dimers (middle, Scheme 1) form via reactions of gaseous  $CH_3OH$  with neutral  $CH_3OH$  monomers (left, Scheme 1) and then reorient to properly align the orbitals involved in the kinetically relevant elimination step (right, Scheme 1).

DFT estimates of  $CH_3OH$  dehydration routes on small zeolite cluster models (3 T-atoms) previously showed that these direct routes are preferred over alternate sequential routes, involving methoxide intermediates, also on zeolitic protons [48,49], but such clusters fail to capture van der Waals forces and long-range electrostatic interactions essential for accurate transition state energies within microporous voids. Yet, attractive induced dipole forces, which are not accurately captured by most DFT functionals, should cause an even stronger preference for the larger transition states involved in direct routes, as long as such void spaces are large enough to contain them.  $CH_3OH$  monomers, but not methoxides, were detected in the infrared spectra of H-MFI and H-FAU during contact with  $CH_3OH$  at  $CH_3OH/Al_{Td}$  stoichiometries below unity, while protonated  $CH_3OH$  dimers became evident at higher  $CH_3OH$  contents [50]. The exclusive presence of monomers at low  $CH_3OH$  pressures and the linear increase in dehydration rates with  $CH_3OH$  pressure at these conditions (Fig. 2) provide direct evidence for the involvement of direct routes on H-MFI (see Section S.6 of the Supporting information). Protonated dimers, detected in the infrared spectra of working catalysts at higher  $CH_3OH$  pressures [50], are also consistent with direct dehydration routes and with the zero-order rate dependence observed at high  $CH_3OH$  pressures (Fig. 2). The combination of DFT, infrared and kinetic evidence strongly suggests that zeolite protons catalyze  $CH_3OH$  dehydration through direct routes (Scheme 1).

Direct routes involving quasi-equilibrated  $CH_3OH$  adsorption, protons occupied by H-bonded  $CH_3OH$  monomers or protonated dimers, and  $H_2O$  elimination as the sole kinetically-relevant step lead to the rate equation (Eq. (3)) [19]:

$$\frac{r_{DME}}{[H^+]} = \frac{k_{DME}K_D[CH_3OH]}{1 + K_D[CH_3OH]} = \frac{k_{first}[CH_3OH]}{1 + \frac{k_{first}}{k_{zero}}[CH_3OH]} \quad (3)$$

where  $K_D$  is the equilibrium constant for the adsorption of a  $CH_3OH$  on a H-bonded monomer to form the protonated dimer and  $k_{DME}$  is the rate constant for the formation of DME from protonated dimers (middle, Scheme 1). Measured zero-order rate constants ( $k_{zero}$ ) reflect differences in free energy between the cationic DME formation transition state (right, Scheme 1) and the protonated dimer (middle, Scheme 1). First-order rate constants ( $k_{first}$ ) reflect differences in free energy of the same transition state relative to a gaseous  $CH_3OH$  molecule and an essentially neutral adsorbed  $CH_3OH$  monomer (left, Scheme 1).

Reactions mediated by cationic transition states, as in the case of  $CH_3OH$  dehydration, exhibit activation enthalpies that decrease monotonically with decreasing DPE [35]. When activation entropies do not depend strongly on acid strength, as expected for isostructural polyoxometalate clusters or X-MFI samples, activation free energies will depend linearly (and rate constants exponentially) on DPE values [19,51], as we discuss in the next section.

### 3.4. Influence of acid strength on dehydration rate constants on substituted MFI and POM

Measured  $CH_3OH$  dehydration rate constants are shown as a function of DPE values (calculated on 38T clusters) for X-MFI in Fig. 6. First-order and zero-order rate constants decrease exponentially with increasing DPE, consistent with activation barriers that

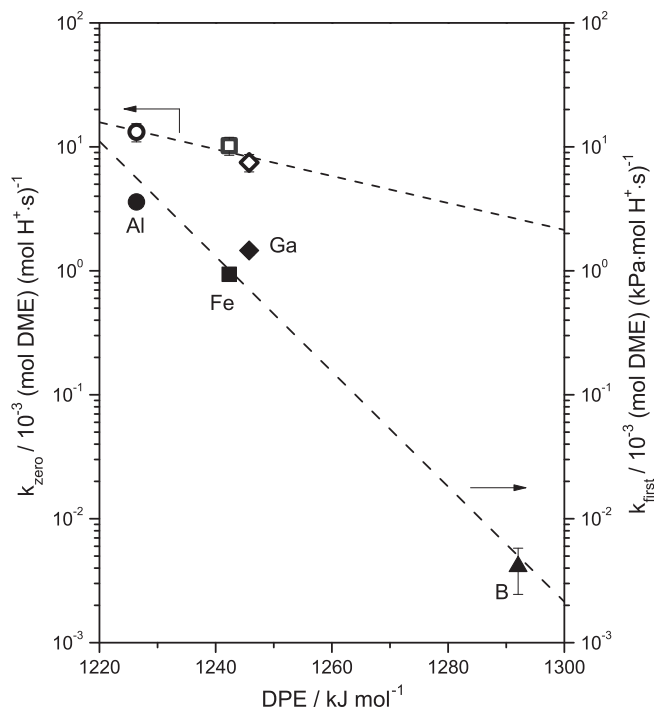


Fig. 6. First-order (closed) and zero-order (open)  $CH_3OH$  dehydration rate constants at 433 K plotted at their respective DPE values calculated on 38 T-atom clusters for H-[Al]-MFI-5 (●), H-[Ga]-MFI (◆), H-[Fe]-MFI (■) and H-[B]-MFI (▲). Dashed lines represent least squares regression of the natural log vs. DPE values. The value of  $k_{zero}$  for B-MFI is unavailable experimentally because of the much higher  $CH_3OH$  pressures required to reach  $CH_3OH$  dimer-saturated surfaces.

increase linearly with increasing DPE for the cationic transition states that mediate these reactions [19,35]. Activation barriers increase with increasing DPE when cationic DME formation transition state energies are more sensitive to changes in electrostatics (reflected in DPE values) than reactive intermediates (Scheme 1), as is the case here because of the higher charge in the DME formation transition states than in CH<sub>3</sub>OH monomers or dimers [19,48].

First-order and zero-order rate constants depend differently on DPE (Fig. 6) because they reflect the energies of uncharged H-bonded CH<sub>3</sub>OH monomers and protonated dimers, respectively, relative to the same cationic transition state (Scheme 1). In the case of first-order rate constants, the transition state is preferentially stabilized over uncharged precursors with decreasing DPE because stronger acid sites are able to stabilize, through electrostatic interactions, cationic species more than less charged species [19]. In the case of zero-order rate constants, the influence of decreasing DPE is attenuated because changes in the electrostatic stabilizations of the cationic transition state and protonated dimer become similar due to their similar charge. Indeed, the Bader charge in the bridging H-atom in protonated CH<sub>3</sub>OH dimer intermediates on POM is near unity (+0.88 to +0.86 e on P and Co POM, respectively) [19], indicating that this species is highly charged and would be stabilized similarly to the cationic transition state with changes in the electrostatic stability of the zeolite conjugate base.

DPE values for Ga-MFI and Fe-MFI differ only slightly (3.4 kJ mol<sup>-1</sup>, 38T clusters) and are within the accuracy of DFT methods ( $\pm 10$  kJ mol<sup>-1</sup> [39]). Measured rate constants are also similar for Ga-MFI and Fe-MFI samples (Fig. 6); the ratios of Ga-MFI to Fe-MFI rate constants are 1.6 and 0.7 for first-order and zero-order rate constants, respectively. The difference in  $k_{\text{first}}$  values is especially small when compared with the nearly 10<sup>6</sup>-fold differences in first-order rate constants among POM and X-MFI samples with DPE values that differ by 212 kJ mol<sup>-1</sup> (Fig. 7). The similar DPE and  $k_{\text{first}}$  values indicate that Ga-MFI and Fe-MFI samples have similar acid strength. This is inconsistent with the conclusions of previous DFT-derived DPE calculations of Ga-MFI and Fe-MFI, which showed DPE differences of up to 20 kJ mol<sup>-1</sup> [5,7,8] probably because of the small clusters used in their calculations (2–8 T-atoms).

Next, we examine how DPE influences values of  $k_{\text{first}}$  on MFI and POM catalysts (Fig. 7). DPE values of POM clusters with W addenda atoms (H<sub>8-n</sub>X<sup>n+</sup>W<sub>12</sub>O<sub>40</sub>; 1080–1143 kJ mol<sup>-1</sup> [19]) depend on the identity of their central atom (X<sup>n+</sup> = P<sup>5+</sup>, Si<sup>4+</sup>, Al<sup>3+</sup> and Co<sup>2+</sup>) and the concomitant change in their number of protons [52]. First-order rate constants on MFI and POM samples both decrease exponentially with increasing DPE (Fig. 7), indicating that in all cases, stronger acids preferentially stabilize the dehydration transition state over the H-bonded CH<sub>3</sub>OH monomer. The slope of the correlation between  $\ln(k_{\text{first}})$  and DPE values for MFI and POM samples is much smaller than unity (Fig. 7), indicating that a large fraction of the energy required to separate the proton is recovered upon formation of the ion-pair at the transition state. The slopes ( $-\text{d}(\ln(k_{\text{first}}))/\text{d}(\text{DPE})$ ) are also similar on POM ( $0.08 \pm 0.06$ ) and MFI ( $0.11 \pm 0.06$ ), leading us to conclude that the fraction of the DPE recovered at the transition state is insensitive to the structure, composition and void space of the solid acid [19].

The values of  $k_{\text{first}}$  predicted from trend lines for POM (Fig. 7) at DPE values of X-MFI 38T clusters (1226–1292 kJ mol<sup>-1</sup>) are much smaller than measured  $k_{\text{first}}$  values on X-MFI samples. In particular, Al-MFI and Co-based POM have similar  $k_{\text{first}}$  values (within a factor of 1.3), but they differ in DPE by 83 kJ mol<sup>-1</sup>. These DPE differences are much larger than expected from inaccuracies in DFT methods ( $\sim 10$  kJ mol<sup>-1</sup>) or the effects of different basis sets ( $\sim 19$  kJ mol<sup>-1</sup>; Section 3.2), suggesting that these differences cannot be explained by differences in basis set size used to calculate DPE on these two systems (DPE values on POM were calculated with a plane wave ba-

sis set and Vanderbilt ultrasoft pseudopotentials [19]). Instead, the larger  $k_{\text{first}}$  values on MFI samples than those expected for hypothetical POM samples with equivalent DPE suggest that the transition state and reactive intermediate energies reflected in  $k_{\text{first}}$  are influenced by interactions that are not described in DPE considerations.

Protons in MFI reside within small voids and adsorb CH<sub>3</sub>OH with much greater enthalpies ( $115 \pm 10$  kJ mol<sup>-1</sup>, microcalorimetry, 400 K, [53]) than estimates for CH<sub>3</sub>OH interactions with protons on POM (62–75 kJ mol<sup>-1</sup> calculated with VASP on Co and P POM, respectively, [19]). This difference is undoubtedly due, in part, to the van der Waals interactions and H-bonding of CH<sub>3</sub>OH with framework O-atoms in MFI as demonstrated by CH<sub>3</sub>OH adsorption enthalpies on silicalite (pure silica MFI) of  $65 \pm 10$  kJ mol<sup>-1</sup> (350 K, microcalorimetry, pure silica MFI [53]). These van der Waals interactions will also stabilize DME formation transition states and to a greater extent than H-bonded CH<sub>3</sub>OH monomers because of its larger size and number of atoms (Scheme 1). Therefore, larger values of  $k_{\text{first}}$  for X-MFI than those of a hypothetical POM sample with the same DPE (by 612-fold at a DPE of 1226 kJ mol<sup>-1</sup>) may be explained, at least partially, by differences in the van der Waals stabilization of the DME formation transition state, which benefits more from tighter confinement than the CH<sub>3</sub>OH monomer. It is not clear, however, to what extent these interactions influence measured rate constants because the DPE values calculated on POM and X-MFI are at different levels of theory and thus are not directly comparable. The preferential solvation of transition states by van der Waals interactions has been explained previously as the “nest effect” in zeolite catalysis [54] and its influence on reactivity is discussed elsewhere [51,55]. We conclude that  $k_{\text{first}}$  values compared on MFI and POM samples indicate that DME formation transition states benefit from confinement in the micropores of MFI.

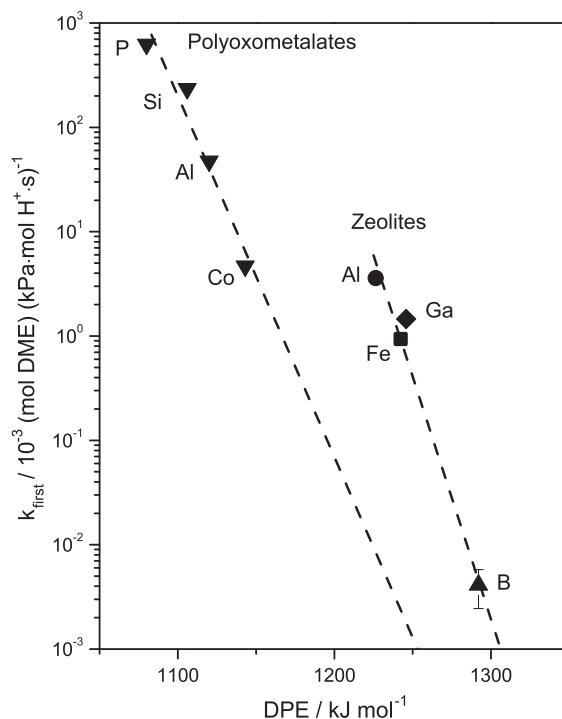


**Fig. 7.** First-order CH<sub>3</sub>OH dehydration rate constants at 433 K plotted at DPE values calculated for 38 T-atom clusters for H-[Al]-MFI-5 (●), H-[Ga]-MFI (◆), H-[Fe]-MFI (■) and H-[B]-MFI (▲), and for H<sub>8-n</sub>X<sup>n+</sup>W<sub>12</sub>O<sub>40</sub>/SiO<sub>2</sub> (in order of increasing DPE: X = P, Si, Al, Co) samples (▲) taken from Carr et al. [19] at their calculated DPE values. Dashed lines represent least squares regression of natural log vs. DPE data.

### 3.5. Al density and acid strength in Al-MFI zeolites

In this section, we examine the effects of Al density on the reactivity of protons in MFI zeolite structures using mechanism-derived CH<sub>3</sub>OH dehydration rate constants to probe how Al density influences the strength and location of Brønsted acid sites. Fig. 8 shows  $k_{zero}$  and  $k_{first}$  as a function of Al or H<sup>+</sup> densities (per unit cell), determined by elemental analysis and pyridine titration, respectively, on Al-MFI samples of different provenance and Si/Al ratio (Table 1). The number of H<sup>+</sup> per unit cell decreases by more than fivefold (3.6–0.7 H<sup>+</sup>/u.c) in these samples (H-[Al]-MFI-1 to H-[Al]-MFI-6; Table 1). The values of  $k_{zero}$  (per H<sup>+</sup>) are similar ( $15 \times 10^{-3} \pm 3 \times 10^{-3}$  DME molecules·(H<sup>+</sup> s)<sup>-1</sup>) on all Al-MFI samples and do not show any discernible monotonic trend with changes in Al or H<sup>+</sup> density (Fig. 8). These data indicate that acid strength is similar in these materials, in view of the fact that zero-order rate constants depend exponentially on DPE (Fig. 6) and are insensitive to confinement differences in MFI voids because of the similar size of DME formation transition states and protonated dimers (Scheme 1 and [19]). This is consistent with similar DPE values calculated at three crystallographically unique tetrahedral Al-substitution sites (within 10 kJ mol<sup>-1</sup>; QM-Pot) [39] and with geometric arguments that support the presence of isolated Al T-atoms in MFI at Si/Al ratios above 9.5 [56]; next-nearest-neighbor Al-atoms decrease the acid strength of associated Brønsted sites [36,57]. First-order rate constants (per H<sup>+</sup>) are similar ( $4.2 \times 10^{-3} \pm 0.6 \times 10^{-3}$  DME molecules·(kPa H<sup>+</sup> s)<sup>-1</sup>) also on MFI samples at H<sup>+</sup>/u.c. densities below 3.6, but are measurably higher on samples with higher Al contents. These data suggest that proton densities below 3.6 H<sup>+</sup>/u.c. do not influence the size of the confining environment around protons, since the consequent solvation effects would influence  $k_{first}$  values because of the significant differences in size between the transition state and the relevant H-bonded CH<sub>3</sub>OH precursors (Section 3.4).

At higher H<sup>+</sup>/u.c. densities in H-[Al]-MFI-1 (3.6 H<sup>+</sup>/u.c.),  $k_{first}$  values are threefold larger than on the other Al-MFI samples (Fig. 8), but  $k_{zero}$  values are similar. Therefore, the higher  $k_{first}$  value at high H<sup>+</sup>/u.c. densities does not reflect a decrease in DPE, because DPE will influence both rate constants (Fig. 6). These differences may instead arise from a change in the solvating environment around H<sup>+</sup>, which affect  $k_{first}$  more than  $k_{zero}$  because of the difference in the size and number of van der Waals contacts of the monomer and dimer species reflected in their values (Scheme 1 and [19]). The increase in dispersive stabilization suggested by larger  $k_{first}$  values reflects a smaller void space near protons at higher H<sup>+</sup>/u.c. densities. Such smaller void spaces arise from (i) occlusion of void space by extra-framework Al (Al<sub>ex</sub>) species, as shown in FAU samples [34]; (ii) van der Waals interactions of transition states with nearby H-bonded CH<sub>3</sub>OH; or (iii) the preferential siting of H<sup>+</sup> (and their associated Al-atoms) within channels instead of intersections in MFI.

Al<sub>ex</sub> contents can be estimated from the difference between H<sup>+</sup> and Al contents (Table 1). This value is actually smaller for H-[Al]-MFI-1 (1.9 Al<sub>ex</sub>/u.c.) than samples with lower  $k_{first}$  values (e.g., H-[Al]-MFI-2; 3.0 Al<sub>ex</sub>/u.c.), inconsistent with occluded Al<sub>ex</sub> as the cause of smaller local voids. In addition, the Al<sub>ex</sub> density (1.9 Al<sub>ex</sub>/u.c.) in H-[Al]-MFI-1 is small compared with the available void volume in MFI (4 intersections/u.c.) and with the Al<sub>ex</sub> density (37 Al<sub>ex</sub>/u.c.; 4 Al<sub>ex</sub>/supercage) in H-USY, for which detrital Al decreases void size and stabilizes transition states [34]. Interactions between H-bonded CH<sub>3</sub>OH and DME formation transition states require protons to be located at distances improbable for these proton densities (3.6 H<sup>+</sup>/u.c.) for the large unit cells of MFI (2.0 × 2.0 × 1.3 nm<sup>3</sup>; [58]) and the number of H<sup>+</sup> binding locations (192 O-atoms/u.c.).

MFI structures contain straight and sinusoidal 10-MR channels (ca. 0.55 nm diameter), which intersect to form ellipsoidal voids (0.64 nm included sphere diameter [59]). The location of Al among these two environments depends sensitively on synthesis protocols and is not always dictated by thermodynamic stability [60,61]. In fact, Al siting in MFI determined from <sup>27</sup>Al MAS NMR [60] and diffraction on Cs-[62–64] and Cu-[65] exchanged MFI show that only a few of the 12 T-sites in MFI contain Al-atoms and that the relative occupancy differs markedly among samples. The similar first-order rate constants in Al-MFI samples with low H<sup>+</sup> density (<3.6 H<sup>+</sup>/u.c.; 5 samples) indicate that H<sup>+</sup> reside within similar environments and, in view of their proclivity for diverse distributions among T-sites, probably within only one of the two possible environments (channels or intersections). We conclude instead that protons first occupy T-sites at channel intersections in these samples. Indeed, 8 out of 12 T-sites in MFI lead to H<sup>+</sup> at such intersections. The preferential siting of H<sup>+</sup> at intersections was inferred from the formation of n-hexane “dimers” at each H<sup>+</sup> for samples with 2.7 H<sup>+</sup>/u.c., which cannot take place at smaller channel locations [66].

The higher  $k_{first}$  value on H-[Al]-MFI-1 compared with samples of lower H<sup>+</sup> density reflects transition state stabilization within more confined spaces, indicating that H<sup>+</sup> become increasingly sited within channels, instead of intersections, as the H<sup>+</sup> density increases. This is consistent with the appearance of a Brønsted ν(OH) band (3656 cm<sup>-1</sup>) in the infrared spectra of H-[Al]-MFI-1 not found in other H-[Al]-MFI samples (Fig. 9; ~3604 cm<sup>-1</sup>), indicating that some H<sup>+</sup> species reside in a different environment than in samples with lower Al contents. These stretching bands have been used previously to distinguish OH species at different O-sites in FAU (sodalite vs. supercage; ~80 cm<sup>-1</sup> difference) [34] and MOR (8-MR vs. 12-MR; ~20 cm<sup>-1</sup> difference) [67]. However, the assignment of ν(OH) frequencies to acid strength or confinement differences is ambiguous because ν(OH) frequencies depend strongly on the local framework geometry at H<sup>+</sup> sites [39]. The adsorption enthalpy of n-butane at a H<sup>+</sup> in the channel intersections in MFI increases by 8 kJ mol<sup>-1</sup> when n-butane points into

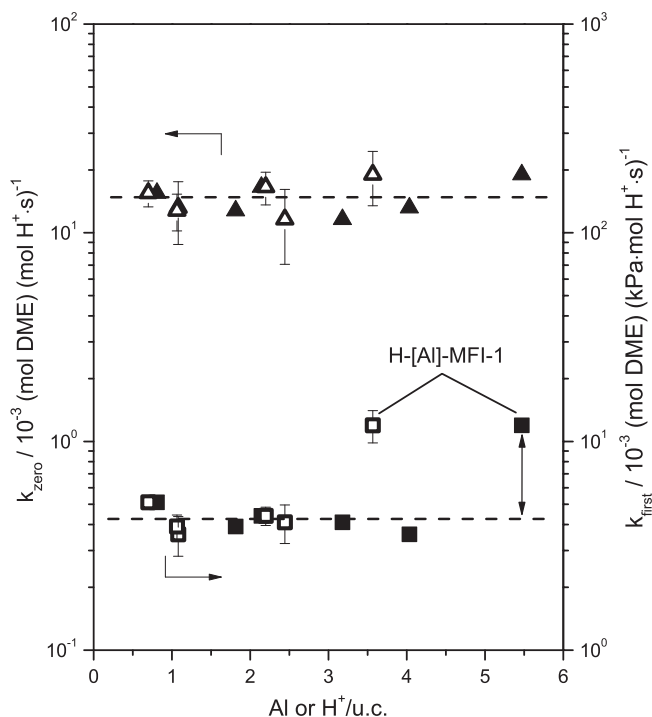


**Fig. 8.** First-order (■) and zero-order (▲) CH<sub>3</sub>OH dehydration rate constants at 433 K on Al-MFI samples of varying provenance and Al (closed) or H<sup>+</sup> (open) densities per unit cell (Table 1; H-[Al]-MFI-1 through 6) determined from elemental analysis and pyridine titrations, respectively. Horizontal dashed lines are provided as a guide to the eye.

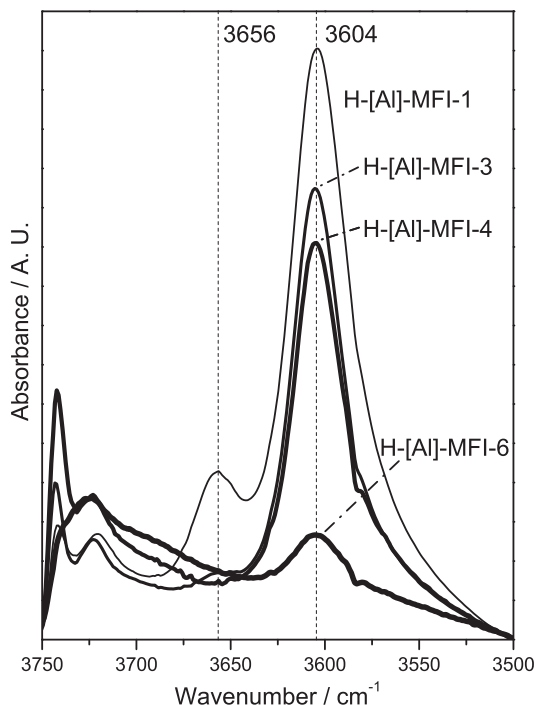


**Fig. 9.** Infrared spectra of H-[Al]-MFI-1, H-[Al]-MFI-3, H-[Al]-MFI-4 and H-[Al]-MFI-6 (identified in Figure) under dynamic vacuum at 433 K.

the sinusoidal, instead of the straight, channel (calculated with DFT; [68]), suggesting that even subtle changes in the  $H^+$ , and thus, the transition state position may be responsible for the threefold difference in  $k_{first}$  (corresponding to a 4 kJ mol<sup>-1</sup> difference in activation free energy barriers at 433 K; see Section S.7 of the Supporting information). We speculate that the presence of four T-atom rings, which seem to correlate empirically with higher Al content zeolites, and which are part of the structural detail at the channel intersections in MFI, might favor preferential location for Al in these voids and explain the siting of Al in channels only after the saturation of these locations at high Al densities.

CH<sub>3</sub>OH dehydration rate constants rigorously reflect the acid strength and void environment of Al-MFI samples of different provenance and  $H^+$  density. Similar values of  $k_{zero}$  over a range of Al/u.c. or  $H^+$ /u.c. densities provide compelling evidence that acid strength is independent of Al and  $H^+$  densities and of  $H^+$  location on Al-MFI samples of different provenance. Values of  $k_{first}$ , however, are larger on an Al-MFI sample with the highest Al density (H-[Al]-MFI-1) indicating that Al preferentially occupies T-sites in channel intersection voids at low Al densities (Si/Al > 23) and populates locations within channels only at higher proton densities.

#### 4. Conclusions

The mechanistic interpretation of CH<sub>3</sub>OH dehydration rate constants per proton clarifies the effects of the identity (Al<sup>3+</sup>, Ga<sup>3+</sup>, Fe<sup>3+</sup>, B<sup>3+</sup>), concentration and location of heteroatoms on acid strength and solvation on a series of MFI samples. DFT-derived deprotonation energies (DPE; calculated rigorously on large clusters to mitigate the effects of cluster termination) capture the changes in electrostatic stability that, in turn, influence the stability of DME formation transition states reflected in CH<sub>3</sub>OH dehydration rate constant values on POM and MFI samples of different composition. Equivalent first-order and zero-order rate constants on a series of Al-MFI samples with a wide range of  $H^+$  densities (0.7–2.4  $H^+$ /u.c.) indicate that acid strength and  $H^+$  location are

independent of acid site concentration. The abrupt increase in first-order but not zero-order rate constants for samples with high  $H^+$  density (3.6  $H^+$ /u.c.) provides evidence for the preferential siting of  $H^+$  in the channel intersection void of MFI and the ultimate placement of  $H^+$  in channels only at these high site densities.

First-order rate constants decreased exponentially with DPE on X-MFI and W-based polyoxometalate (POM) solid acids to similar extents, indicating the ubiquitous influence of DPE on the stability of DME formation transition states and relevant precursors regardless of catalyst structure or composition. Larger first-order rate constants on X-MFI than hypothetical POM samples at similar DPE values reflect the enzyme-like confinement and van der Waals stabilization of DME formation transition states in the microporous voids of X-MFI samples.

These findings reveal the fundamental and substantial influence of acid strength and solvation on the reactivity of solid Brønsted acids. First-order and zero-order rate constants measured on X-MFI samples and combined with rigorous DPE calculations clear up controversies surrounding the acid strength of MFI and indicate that heteroatom composition, and not density, influences the acid strength of X-MFI.

#### Acknowledgments

The authors thank Dr. Rajamani Gounder (Caltech) and Dr. David Hibbits (UC Berkeley) for helpful technical discussions throughout the course of these studies, Prof. Raul F. Lobo (Univ. of Delaware) for the Silicalite-1 sample, and Dr. Sonjong Hwang (Caltech) for the NMR spectra. We gratefully acknowledge the financial support for this research from the Chevron Energy Technology Company. AJ acknowledges a graduate research fellowship from the National Science Foundation. Supercomputing resources were provided by the Molecular Graphics and Computation Facility in the College of Chemistry at the University California, Berkeley under NSF CHE-0840505. We also thank Dr. George D. Meitzner for his technical comments and editing of this manuscript.

#### Appendix A. Supplementary material

Supplementary data associated with this article can be found, in the online version, at <http://dx.doi.org/10.1016/j.jcat.2014.01.007>.

#### References

- [1] J. Čejka, G. Centi, J. Perez-Pariente, W.J. Roth, *Catal. Today* 179 (2012) 2–15.
- [2] A. Corma, *Chem. Rev.* 95 (1995) 559–614.
- [3] J. Čejka, A. Corma, S. Zones, *Zeolites and Catalysis: Synthesis, Reactions and Applications*, John Wiley & Sons, 2010.
- [4] H.V. Bekkum, *Introduction to Zeolite Science and Practice*, Elsevier, 2001.
- [5] A. Chatterjee, T. Iwasaki, T. Ebina, A. Miyamoto, *Micropor. Mesopor. Mater.* 21 (1998) 421–428.
- [6] R. Zahradnik, P. Hobza, B. Wichterlova, J. Čejka, *Collect. Czech. Chem. Commun.* 58 (1993) 2474–2488.
- [7] P. Strodel, K.M. Neyman, H. Knözinger, N. Rösch, *Chem. Phys. Lett.* 240 (1995) 547–552.
- [8] S.P. Yuan, J.G. Wang, Y.W. Li, H. Jiao, *J. Phys. Chem. A* 106 (2002) 8167–8172.
- [9] S. Jungstittwong, J. Lomratsiri, J. Limtrakul, *Int. J. Quantum Chem.* 111 (2011) 2275–2282.
- [10] H.V. Brand, L.A. Curtiss, L.E. Iton, *J. Phys. Chem.* 97 (1993) 12773–12782.
- [11] H.V. Brand, L.A. Curtiss, L.E. Iton, *J. Phys. Chem.* 96 (1992) 7725–7732.
- [12] D.J. Parrillo, R.J. Gorte, *J. Phys. Chem.* 97 (1993) 8786–8792.
- [13] S.M. Babitz, B.A. Williams, J.T. Miller, R.Q. Snurr, W.O. Haag, H.H. Kung, *Appl. Catal. A* 179 (1999) 71–86.
- [14] W.F. Kladnig, *J. Phys. Chem.* 83 (1979) 765–766.
- [15] A.I. Biaglow, R.J. Gorte, G.T. Kokotailo, D. White, *J. Catal.* 148 (1994) 779–786.
- [16] J.A. Lercher, C. Grundling, G. Eder-Mirth, *Catal. Today* 27 (1996) 353–376.
- [17] R.J. Gorte, *Catal. Lett.* 62 (1999) 1–13.
- [18] D.J. Parrillo, C. Lee, R.J. Gorte, D. White, W.E. Farneth, *J. Phys. Chem.* 99 (1995) 8745–8749.
- [19] R.T. Carr, M. Neurock, E. Iglesia, *J. Catal.* 278 (2011) 78–93.
- [20] D.W. Fickel, A.M. Shough, D.J. Doren, R.F. Lobo, *Micropor. Mesopor. Mater.* 129 (2010) 156–163.

- [21] W.E. Stewart, M. Caracotsios, *Athena Visual Studio* 14 (2010) 2.
- [22] J.D. Chai, M. Head-Gordon, *PCCP* 10 (2008) 6615–6620.
- [23] M.J. Frisch, G.W. Trucks, H.B. Schlegel, G.E. Scuseria, M.A. Robb, J.R. Cheeseman, G. Scalmani, V. Barone, B. Mennucci, G.A. Petersson, H. Nakatsuji, M. Caricato, X. Li, H.P. Hratchian, A.F. Izmaylov, J. Bloino, G. Zheng, J.L. Sonnenberg, M. Hada, M. Ehara, K. Toyota, R. Fukuda, J. Hasegawa, M. Ishida, T. Nakajima, Y. Honda, O. Kitao, H. Nakai, T. Vreven, J.A. Montgomery, J.E. Peralta, F. Ogliaro, M. Bearpark, J.J. Heyd, E. Brothers, K.N. Kudin, V.N. Staroverov, R. Kobayashi, J. Normand, K. Raghavachari, A. Rendell, J.C. Burant, S.S. Iyengar, J. Tomasi, M. Cossi, N. Rega, J.M. Millam, M. Klene, J.E. Knox, J.B. Cross, V. Bakken, C. Adamo, J. Jaramillo, R. Gomperts, R.E. Stratmann, O. Yazyev, A.J. Austin, R. Cammi, C. Pomelli, J.W. Ochterski, R.L. Martin, K. Morokuma, V.G. Zakrzewski, G.A. Voth, P. Salvador, J.J. Dannenberg, S. Dapprich, A.D. Daniels, Farkas, J.B. Foresman, J.V. Ortiz, J. Cioslowski, D.J. Fox, *Gaussian 09, Revision C.01*, Wallingford CT, 2009.
- [24] D.H. Olson, G.T. Kokotailo, S.L. Lawton, W.M. Meier, *J. Phys. Chem.* 85 (1981) 2238–2243.
- [25] S. Svelle, C. Tuma, X. Rozanska, T. Kerber, J. Sauer, *J. Am. Chem. Soc.* 131 (2009) 816–825.
- [26] J. Sauer, in: G. Pacchioni, P. Bagus, F. Parmigiani (Eds.), *Cluster Models for Surface and Bulk Phenomena*, Plenum Press, New York, 1992.
- [27] J. Gomes, P.M. Zimmerman, M. Head-Gordon, A.T. Bell, *J. Phys. Chem. C* 116 (2012) 15406–15414.
- [28] H. Bludau, H.G. Karge, W. Niessen, *Micropor. Mesopor. Mater.* 22 (1998) 297–308.
- [29] C.A. Emeis, *J. Catal.* 141 (1993) 347–354.
- [30] C.D. Baertsch, K.T. Komala, Y.H. Chua, E. Iglesia, *J. Catal.* 205 (2002) 44–57.
- [31] B.H. Wouters, T.H. Chen, P.J. Grobet, *J. Am. Chem. Soc.* 120 (1998) 11419–11425.
- [32] J.A. van Bokhoven, N. Danilina, *Zeolites and Catalysis*, Wiley-VCH Verlag GmbH & Co, KGaA, 2010, pp. 283–300.
- [33] B. Xu, F. Rotunno, S. Bordiga, R. Prins, J.A. van Bokhoven, *J. Catal.* 241 (2006) 66–73.
- [34] R. Gounder, A.J. Jones, R.T. Carr, E. Iglesia, *J. Catal.* 286 (2012) 214–223.
- [35] A.M. Rigby, G.J. Kramer, R.A. vanSanten, *J. Catal.* 170 (1997) 1–10.
- [36] L. Grajciar, C.O. Arean, A. Pulido, P. Nachtigall, *PCCP* 12 (2010) 1497–1506.
- [37] C. Lo, B.L. Trout, *J. Catal.* 227 (2004) 77–89.
- [38] M. Brandle, J. Sauer, *J. Am. Chem. Soc.* 120 (1998) 1556–1570.
- [39] U. Eichler, M. Brandle, J. Sauer, *J. Phys. Chem. B* 101 (1997) 10035–10050.
- [40] P.G. Moses, J.K. Nørskov, *ACS Catal.* 3 (2013) 735–745.
- [41] M. Leslie, M.J. Gillan, *J. Phys. C-Solid State Phys.* 18 (1985) 973–982.
- [42] C. Freysoldt, J. Neugebauer, C.G. Van de Walle, *Phys. Rev. Lett.* 102 (2009).
- [43] R. Shannon, *Acta Crystallogr. Sect. A* 32 (1976) 751–767.
- [44] R.G. Pearson, *Inorg. Chem.* 27 (1988) 734–740.
- [45] J. Macht, R.T. Carr, E. Iglesia, *J. Catal.* 264 (2009) 54–66.
- [46] W. Tang, E. Sanville, G. Henkelman, *J. Phys.-Condes. Matter* 21 (2009).
- [47] R. Pophale, P.A. Cheeseman, M.W. Deem, *PCCP* 13 (2011) 12407–12412.
- [48] S.R. Blazzkowski, R.A. vanSanten, *J. Phys. Chem. B* 101 (1997) 2292–2305.
- [49] S.R. Blazzkowski, R.A. vanSanten, *J. Am. Chem. Soc.* 118 (1996) 5152–5153.
- [50] A. Zecchina, S. Bordiga, G. Spoto, D. Scarano, G. Spano, F. Geobaldo, *J. Chem. Soc.-Faraday Trans.* 92 (1996) 4863–4875.
- [51] R. Gounder, E. Iglesia, *Chem. Commun.* 49 (2013) 3491–3509.
- [52] M.J. Janik, J. Macht, E. Iglesia, M. Neurock, *J. Phys. Chem. C* 113 (2009) 1872–1885.
- [53] C.C. Lee, R.J. Gorte, W.E. Farneth, *J. Phys. Chem. B* 101 (1997) 3811–3817.
- [54] E.G. Derouane, *J. Catal.* 100 (1986) 541–544.
- [55] R. Gounder, E. Iglesia, *Acc. Chem. Res.* 45 (2012) 229–238.
- [56] D. Barthomeuf, *Mater. Chem. Phys.* 17 (1987) 49–71.
- [57] A. Corma, *Curr. Opin. Solid State Mater. Sci.* 2 (1997) 63–75.
- [58] C.M. Baerlocher, L.B. McCusker, *Database of Zeolite Structures*, 2013. <<http://www.iza-structure.org/databases/>>.
- [59] M.D. Foster, I. Rivin, M.M.J. Treacy, O.D. Friedrichs, *Micropor. Mesopor. Mater.* 90 (2006) 32–38.
- [60] S. Sklenak, J. Dedecek, C. Li, B. Wichterlova, V. Gabova, M. Sierka, J. Sauer, *PCCP* 11 (2009) 1237–1247.
- [61] G. Sastre, V. Fornes, A. Corma, *J. Phys. Chem. B* 106 (2002) 701–708.
- [62] C.W. Kim, N.H. Heo, K. Seff, *J. Phys. Chem. C* 115 (2011) 24823–24838.
- [63] D.H. Olson, N. Khosrovani, A.W. Peters, B.H. Toby, *J. Phys. Chem. B* 104 (2000) 4844–4848.
- [64] J. Dědeček, Z. Sobalík, B. Wichterlová, *Catal. Rev.* 54 (2012) 135–223.
- [65] B.F. Mentzen, G. Bergeret, *J. Phys. Chem. C* 111 (2007) 12512–12516.
- [66] F. Eder, M. Stockenhuber, J.A. Lercher, *J. Phys. Chem. B* 101 (1997) 5414–5419.
- [67] R. Gounder, E. Iglesia, *J. Am. Chem. Soc.* 131 (2009) 1958–1971.
- [68] B.A. De Moor, M.F. Reyniers, O.C. Gobin, J.A. Lercher, G.B. Marin, *J. Phys. Chem. C* 115 (2011) 1204–1219.